First-Principles Study on Electronic and Thermal Transport Properties of FeRuTiX Quaternary Heusler Compounds (X=Si, Ge, Sn)

Saurabh Singh, Shubham Singh, Bhuvanesh Srinivasan, Ashish Kumar, Nitinkumar Bijewar, Takao Mori, Tsunehiro Takeuchi, Jean-françois Halet

WILEY-VCH

ARTICLE

First-Principles Study on Electronic and Thermal Transport Properties of FeRuTiX Quaternary Heusler Compounds (X = Si, Ge, Sn)

Saurabh Singh*, Shubham Singh, Bhuvanesh Srinivasan*, Ashish Kumar, Nitinkumar Bijewar, Takao Mori, Tsunehiro Takeuchi and Jean-François Halet*

Dedicated to a long-time friend, Professor Antoine Maignan on the occasion of his 60th birthday.

Keywords: electronic structure; quaternary Heusler alloy; semiconductor; thermoelectrics; thermal properties

Abstract: The structural, electronic, thermal and lattice thermal transport properties of the three hypothetical quaternary Heusler alloys FeRuTiX (X = Si, Ge, Sn) were investigated with the aid of first-principles calculations. All compounds were found to be semiconducting with a small indirect band gap. Flat bands near the conduction band edge and degenerate multi-bands near the valance band edge suggest that these systems should exhibit both large Seebeck coefficients and good electrical conductivity. The analysis of the calculated vibrational spectra showed that the three compounds are thermodynamically stable. The computed lattice thermal conductivity indicates that among the three compounds that of FeRuTiSn is rather low at high temperature. Indeed, a low lattice thermal conductivity (~3.5 $Wm^{-1}K^{-1}$ at 1000 K) together with a small electronic band gap (0.51 eV) with an appropriate electronic structure (disperse and flat bands) render FeRuTiSn a promising candidate as a high-temperature thermoelectric material.

***Corresponding Authors: Saurabh Singh,** Research Center for Smart Energy Technology, Toyota Technological Institute, Nagoya 468-8511, Japan. CREST, Japan Science and Technology Agency, Tokyo 102-0076, Japan. MIRAI, Japan Science and Technology Agency, Tokyo 102-0076, Japan. E-mail: saurabhsingh950@gmail.com; **Bhuvanesh Srinivasan,** WPI International Center for Materials Nanoarchitectronics (WPI-MANA), National Institute for Materials Science (NIMS), 1-1 Namiki, Tsukuba, 305-0044, Japan. CNRS–Saint-Gobain–NIMS, IRL 3629, Laboratory for Innovative Key Materials and Structures (LINK), National Institute for Materials Science (NIMS), 1-1 Namiki, Tsukuba 305-0044, Japan; Department of Metallurgical and Materials Engineering, Indian Institute of Technology Madras (IIT-Madras), Chennai 600 036, India. E-mail: bhuvanesh.srini@iitm.ac.in; **Jean-François Halet,** CNRS–Saint-Gobain–NIMS, IRL 3629, Laboratory for Innovative Key Materials and Structures (LINK), National Institute for Materials Science (NIMS), 1-1 Namiki, Tsukuba 305-0044, Japan. E-mail: Jean-Francois.Halet@univ-rennes1.fr

Shubham Singh, Physical Science and Engineering Division (PSE), King Abdullah University of Science and Technology (KAUST), Thuwal, Saudi Arabia

Ashish Kumar, Department of Physics (SoE), University of Petroleum and Energy Studies (UPES), Bidholi, Dehradun - 248007, India

Nitinkumar Bijewar, Department of Physics, University of Mumbai, Kalina Campus, Santacruz (E) Mumbai- 400098, India

Takao Mori, WPI International Center for Materials Nanoarchitectronics (WPI-MANA), National Institute for Materials Science (NIMS), 1-1 Namiki, Tsukuba, 305-0044, Japan

Tsunehiro Takeuchi, Research Center for Smart Energy Technology, Toyota Technological Institute, Nagoya 468-8511, Japan. CREST, Japan Science and Technology Agency, Tokyo 102-0076, Japan. MIRAI, Japan Science and Technology Agency, Tokyo 102-0076, Japan.

1 Introduction

For thermoelectric applications, i.e., converting waste heat into electricity, good materials are selected on the basis of the magnitude of their dimensionless figure of merit, ZT, which is directly related to the conversion efficiency [1–6]. ZT is defined as $(S^2\sigma T)/\kappa$, where S is the Seebeck coefficient, σ is the electrical conductivity, T is the absolute temperature, and κ is the total thermal conductivity (the sum of the electronic contribution, κ_e, and the lattice contribution, κ_l) of the compound [1, 7]. Consequently, for a large efficiency, a material should exhibit high ZT values which require large S and σ, and small κ. This condition is very challenging to fulfill since S, σ, and κ_e are interrelated and depend all on the carrier concentration, n. Indeed, assuming the empirical Wiedemann-Franz law, $\kappa_e = L\sigma T$, where L is the Lorentz number, the electronic thermal conductivity is affected by the change of the electronic structure upon the optimization of the power factor ($PF = S^2\sigma$) [1, 7]. On the other hand, κ_l solely depends upon the lattice environment, and phonon engineering and lattice softening play a very effective role in diminishing or even suppressing the lattice thermal conductivity through atomic disordering, heavy mass element substitutions, lowering the dimension from 3D to 2D or 1D, and nano-structuring [8-14]. Thanks to both numerous experimental and computational investigations, all these aspects have been successfully applied to many Heusler alloys to improve their figure of merit [8–10, 16–27].

Indeed, over the last several decades, Heusler alloys have been studied extensively due to their wide range of applications in spintronic, magnetic, superconducting, mechanical [28] and thermoelectric areas to mention a few [29–35]. Based on their chemical formula and atomic arrangements of the constituting elements, the large class of Heusler compounds can be broadly classified into three categories: half-Heusler (general formula ABC), full-Heusler (A_2BC), and quaternary Heusler ($AA'BC$) compounds [29–42]. Their properties can often be predicted simply by counting the number of their valence electrons [43, 44]. For instance, the quaternary Heusler alloys, referred to as QHAs, can display metallic, half-metallic, non-magnetic, magnetic and semiconducting properties depending on the valence electron

count per formula [36,38, 45–48]. From the thermoelectric point of view, some QHAs can exhibit favorable electronic (semiconducting ground state with band gap values in the range of 0.5 – 1.0 eV) and lattice degrees of freedom for tailoring interesting thermoelectric properties for high-temperature applications [36, 38, 49–54]. For example, cobalt-based QHAs with half-metallic/semiconducting electronic structures have been reported [55–60]. Half-metallic QHAs have also been proposed for their promising electronic, magnetic, and thermoelectric properties due to their high power factors [55–63].

In the search for new thermoelectric materials, first-principles calculations can play a complementary role in both predicting new materials properties, as well as providing a theoretical basis for observed phenomena [64]. Benefits of first-principles exploratory research has been illustrated for some half-Heusler thermoelectrics [67, 68]. Some QHAs have also come into view as potential thermoelectric candidates on the basis of theoretical studies [69]. Though there are numerous options for selecting elements to propose novel QHAs, Fe–Si-based Heusler alloys are particularly attractive due to their cheap, non-toxic, and earth plentiful nature, and their robust chemical and thermal stability [70–72]. In addition, the formation of hybridized Fe 3*d*–Si 3*p* electronic states near the Fermi level should make them suitable for reasonable transport properties [17]. Indeed, computations on hypothetical 24-valence-electron QHAs of formula FeRuTiX (X = Si, Ge, Sn) have shown non-magnetic ground states with a small energy bandgap (0.5 – 0.6 eV), one of the prerequisites for promising thermoelectric properties [3, 38, 73–75]. Not long ago we ourselves theoretically looked at the thermoelectric properties of FeRuTiSi, in particular the electronic thermal conductivity, proposing a large potential value of *ZT* close to unity for this hypothetical QHA [74]. High thermal conductivity, which can be as high as 10 $Wm^{-1}K^{-1}$, is one important drawback for high *ZT* in Heusler materials [77] and therefore knowing the thermal conductivity can provide more realistic information on computed *ZT* of hypothetical QHAs. Thus, detailed electronic and phonon structure calculations for thermal stability and practical applicability of these compounds for thermoelectric applications are highly desirable [77]. Using first-principles calculations, we have investigated the thermodynamical stability, the electronic and vibrational structures, as well as the thermal transport properties of the hypothetical FeRuTiX QHAs (X = Si, Ge, Sn) which are reported first time to the best of our knowledge.

2 Results and discussion

2.1 Structural properties

The unit cell of FeRuTiX (X = Si, Ge, Sn) is shown in Figure 1a. To estimate the equilibrium lattice parameters, calculations of self-consistency energies with a set of different volumes of the unit cell were first performed for each compound using the PBE and TB-mBJ exchange-correlation functionals (see Section 4 for the computational details). We checked the most stable crystal structure for FeRuTiX (X = Si, Ge, Sn) alloys with three different possible configurations, T_I: Fe (1/4, ¼, ¼), Ru (1/2, ½, ½), Ti (3/4, ¾, 3/4), X (0, 0, 0); T_{II}: Fe (1/4, ¼, ¼), Ru (3/4, ¾, ¾), Ti (1/2, ½, ½), X (0, 0, 0); and T_{III}: Fe (1/2, ½, ½), Ru (1/4, ¼, ¼), Ti (3/4, ¾, ¾), X (0, 0, 0), as described in an earlier report by Kundu et al. [38]. The comparison of the total energy obtained from the SCF calculations shown in Figure 1b, 1c, 1d clearly suggests that type two (T_{II}) structure is energetically more stable than the other types, i.e, T_I and T_{III} for all FeRuTiX QHAs (X = Si, Ge, Sn) compounds. Therefore, we have further considered the most stable structure, i.e., type T_{II}, for the calculations of structural, electronic and thermal properties. The energy vs. volume plots for all three compounds are shown in Figure 1e, 1f, and 1g. The computed equilibrium lattice constants (a_0) and bulk modulii (B_0) are reported in Table 1. As expected, the equilibrium cell parameter increases with the size of the main-group element. It is in the range of the lattice constants experimentally observed for comparable QHAs such as CoRhMnGe (a_0 = 5.89 Å), CoRhMnGa (a_0 = 5.976 Å), CoRhMnSn (a_0 = 6.149 Å), CoRhMnSb (a_0 = 6.048 Å) [90, 91].

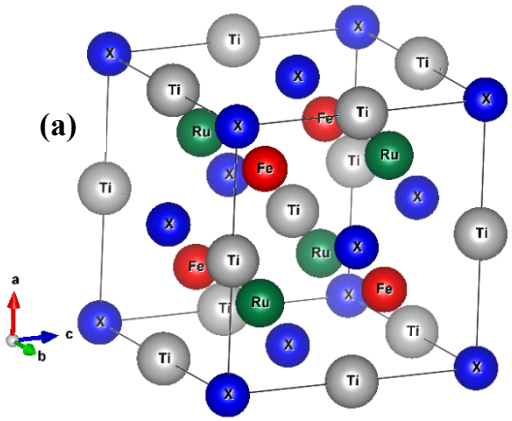

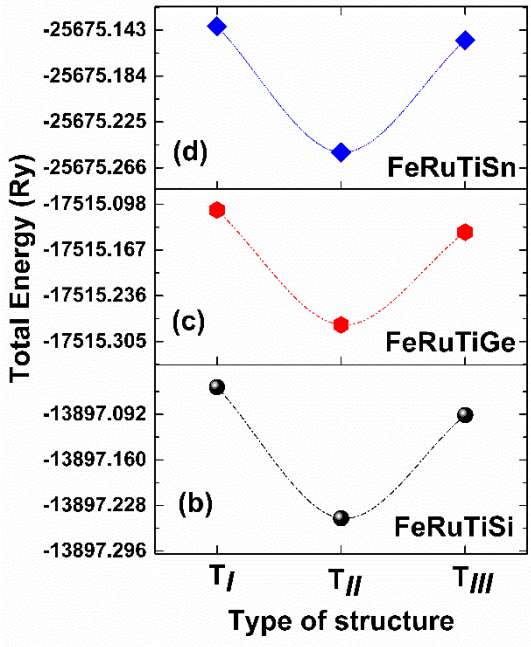

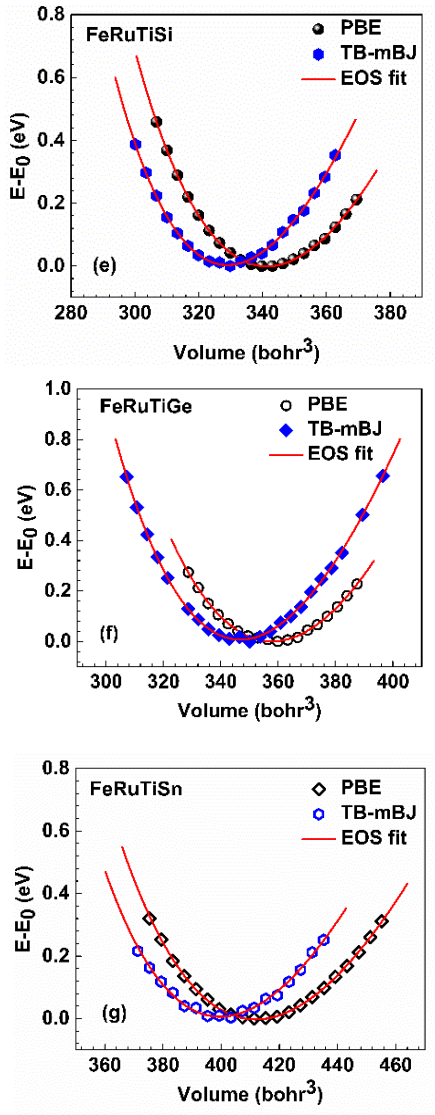

Figure 1. (a) Unit cell of FeRuTiX (X = Si, Ge, Sn), (b-d) total energy of FeRuTiX (X = Si, Ge, Sn) compounds with different structural configurations, and energy vs. volume curves for (e) FeRuTiSi, (f) FeRuTiGe, and (g) FeRuTiSn. The solid symbols represent the calculated energy values, and the solid lines are the fitting curves of the equation of states.

The calculated values of the lattice constant using GGA functional for other similar QHAs, with cubic crystal structure containing Fe, Ru, Si, Ge as constituent elements, have similar lattice constant in the range of 5.7 – 6.3 Å [39, 60-73]]. However, the electronic structure shows different features including metallic, semi-metallic, half-metallic, and semiconductors with a large variation in the value of band gaps and magnetic moments [39]. The calculated values of the total energy are found to be higher for the spin-polarized calculations as compared to non-spin polarized ones for all the considered systems. This confirms that all these compounds are non-magnetic. For all the three systems, the equilibrium lattice constants computed with the PBE functional are found to be slightly larger (ca. 1%) than those computed with the the TB-mBJ functional. Such a small overestimation of PBE-computed cell parameters in comparison to the TB-mBJ computed ones was already noticed in the case of full-Heusler compounds [83]. We noted that our PBE-computed values are ca. 1% larger than those obtained by Guo *et al.* using the same PBE exchange-correlation functional but a different DFT code [73].

Table 1: Calculated lattice constant a_0, bulk modulus B_0, and bandgap (E_g) for FeRuTiX compounds (X = Si, Ge, Sn) using the PBE and TB-mBJ exchange-correlation functionals.

Compound	Lattice constant a_0 (Å)		Bulk modulus B_0 (GPa)		Energy band gap E_g (eV)	
Functional	PBE	TB-mBJ	PBE	TB-mBJ	PBE	TB-mBJ
FeRuTiSi	5.871 5.84[73]	5.804	226.29	260.16	0.32 0.40	0.59
FeRuTiGe	5.964 5.93[73]	5.897	221.74	246.85	0.18 0.21	0.55
FeRuTiSn	6.186 6.19[73]	6.124	205.28	232.13	0.03 0.09	0.51

The calculated equilibrium bulk modulus (B_0) values slightly diminish going from Si to Sn for both functionals (Table 1). We noted that if the TB-mBJ functional gave slightly smaller equilibrium lattice constants with respect to PBE, it overestimates somewhat the equilibrium bulk modulii (ca. 12–15%). The difference in bulk modulus values using two different exchange-correlation functionals is due to the difference in the energy vs. volume curvature obtained for each compound.

2.2 Electronic structure analysis

The total density of states (DOS) using the computed equilibrium lattice parameters of the three compounds was estimated employing both the PBE and TB-mBJ functionals. The values of the computed band gap for each compound are reported in Table 1. All the compounds show a small bandgap indicating a semiconducting ground state character as reported earlier [73]. With the PBE functional – which generally underestimates bandgaps, the bandgap values are 0.32, 0.18, and 0.03 eV for FeRuTiSi, FeRuTiGe, and FeRuTiSn, respectively. These values are slightly lower than the values reported earlier by Guo *et al.* (shown in Table 1) using a different DFT code [73]. As expected, larger bandgap values are computed using the TB-mBJ functional, which are 0.59, 0.55, and 0.51 eV for FeRuTiSi, FeRuTiGe, and FeRuTiSn, respectively, values which are 'good' values for thermoelectric materials. Both functionals show a decreasing trend in the bandgap from Si- to Ge- to Sn-containing QHAs. This

10.1002/zaac.202300080

is consistent with the augmentation of the covalent character between the metals and non-metals as we move from Si to Sn.

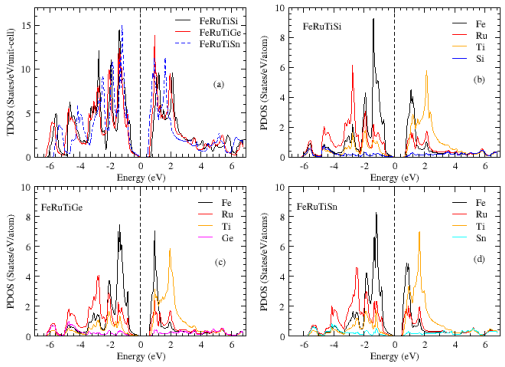

Figure 3. (a) Total density of states (TDOS), and atom-projected DOS shown are (b) FeRuTiSi, (c) FeRuTiGe, and (d) FeRuTiSn computed with the TB-mBJ functional.

The shapes of the PBE- and TB-mBJ-computed total DOS are nearly identical. They just differ by the fact that the conduction band (CB) is shifted to higher energy with respect to that of the former (Figure 2).

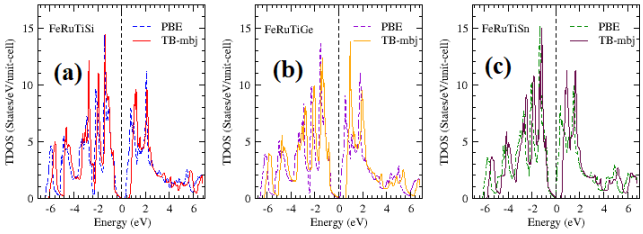

Figure 2. Total density of states for FeRuTiSi (a), FeRuTiGe (b), and FeRuTiSn (c).

Since it is known that the TB-mBJ functional provides rather accurate bandgaps, we continue the analysis of the electronic structure using only the TB-mBJ results [80-82]. Atom-projected densities of states (PDOS) are shown in Figure 3. The top of the valence band (VB) and the bottom of the conduction band (CB) are mainly Fe in character. Sharp peaks of DOS should be good for large Seebeck coefficients. The Ti and Ru contributions are more spread out in energy which should feature good electrical properties. Strong covalence between metal and non-metal atoms reflects in the non-metal contribution which is largely spread out all over the VB and CB. To know the effective role of the band character in transport properties, the electronic band dispersion was also analyzed along some high-symmetry lines of the first Brillouin zone (BZ) (Figure 4) [90, 91]. The band structure confirms semiconducting properties with an indirect band gap between a valence-band maximum at *Γ* and a conduction band minimum at *X* for all the three compounds. A triply degenerate-state situation is observed for the VB at *Γ*, whereas a more complex situation occurs for the CB at *X* with degenerate (X = Ge) or nearly degenerate bands (X = Si, Sn). Note that flat bands are computed at the bottom of the CB which should manifest in high effective masses and therefore large and negative Seebeck coefficients for these compounds [83].

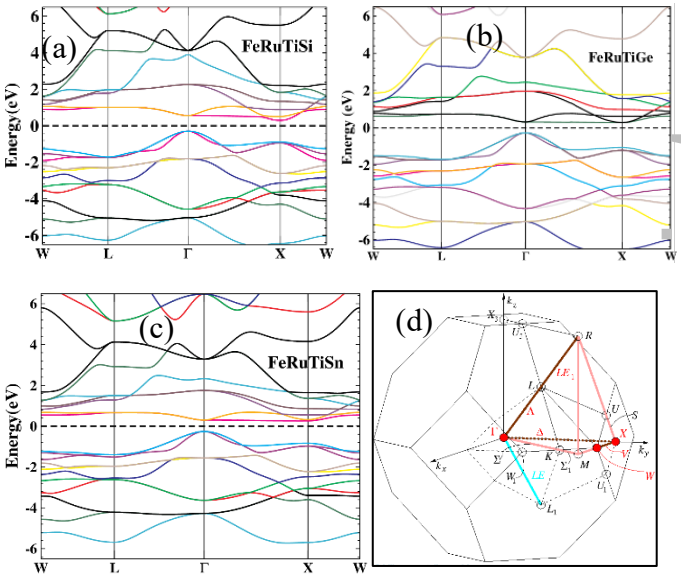

Figure 4. Electronic band dispersion plots for FeRuTiSi (a), FeRuTiGe (b), and FeRuTiSn (c) computed with the TB-mBJ functional. See the Brillouin zone (d) for the corresponding symmetry lines *W* – *L* – *Γ* – *X* – *W* (d) [92, 93].

2.3 Phonon structure analysis

The phonon dispersion and phonon density of states (phonon-DOS) for FeRuTiSi, FeRuTiGe, and FeRuTiSn were calculated using the PBE exchange correlation functional for more expedient computations. Figure 5 shows the phonon dispersion plots along some high-symmetry lines in the first BZ (see Figure 4 for the corresponding BZ) [92, 93]. All vibrational spectra show real frequencies, suggesting that all the three compounds are thermodynamically stable (at least at 0 K) in the cubic phase generally encountered for QHAs. Three acoustic modes are found at low energy in the 0 to ~20 meV range below several optical modes (energy > 20 meV). Among the former, two modes are doubly degenerate along the *Γ* – *X* and *Γ* – *L* directions for all three compounds. The degeneracy is lifted out along the *W* – *L* symmetry line. It is clearly visible that the set of both acoustic and optical vibration modes are more constrained in energy and softer as we go from Si to Sn (Figure 5). This was expected because of the frequency (energy) and mass relationship. In comparison to the Si and Ge, the mass of the Sn is larger. Indeed, within the harmonic approximation, the vibrational frequencies are inversely proportional to the square root of the mass [i.e., $\omega \propto \sqrt{(k/m)}$ with ω, the frequency, *k* the stiffness, and *m* the mass] of the

constituting elements of the compounds. Inversely, the light mass elements contribute to the upper optical branch modes found around 50 meV for FeRuTiSi, 40 meV for FeRuTiGe, and 33 meV for FeRuTiSn.

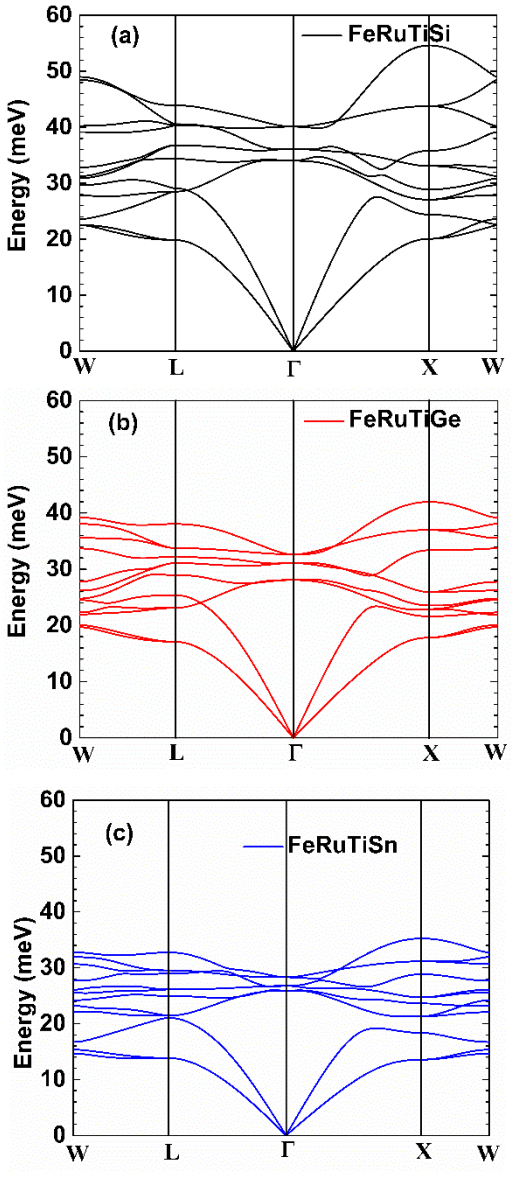

Figure 5. PBE-computed phonon dispersion plots for FeRuTiSi (a), FeRuTiGe (b), and FeRuTiSn (c).

The total and atom-projected phonon-DOS for the three compounds are shown in Figure 6. It is evident that the acoustic phonon modes which are important for thermal transport because of their larger sound velocity, mostly involve vibrations of the heavier elements. The phonon-DOS at very low energy is larger in the case of FeRuTiSn with respect to FeRuTiSi and FeRuTiGe. Consequently, the lowest thermal conductivity among these three compounds is expected for the former.

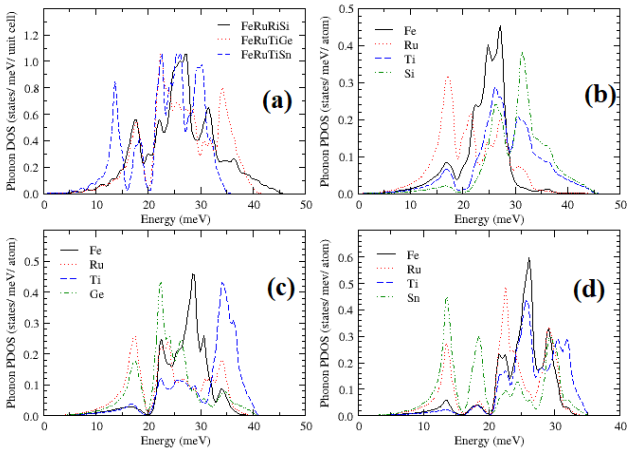

Figure 6. Total (a) and atom-projected (b, c, d) vibrational density of states of FeRuTiSi, FeRuTiGe, and FeRuTiSn, respectively.

2.4 Thermal properties and lattice thermal conductivity

The thermal properties, namely the Helmholtz free energy (*F*), entropy (*S*), and constant volume-specific heat (C_V) were computed as a function of temperature for the three compounds from their phonon density of states. The results shown in Figure 7 indicate similar thermal properties for FeRuTiSi and FeRuTiGe. On the other hand, a smaller free energy and a higher entropy are noticed for FeRuTiSn, especially at high temperature. This may be due to higher intensity of phonon-DOS found in the lower energy range observed for FeRuTiSn with respect to FeRuTiSi and FeRuTiGe.

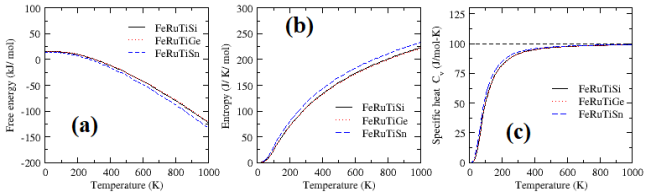

Figure 7. (a) Free energy (*F*), (b) entropy (*S*) and, (c) specific heat at constant volume (C_V) versus the temperature for FeRuTiSi, FeRuTiGe, and FeRuTiSn.

The specific heat calculated for all the compounds approaches the Dulong-Petit limit at high temperature. In the low-temperature

region below 400 K, the magnitude of C_V for FeRuTiSn is slightly higher than for the two other compounds.

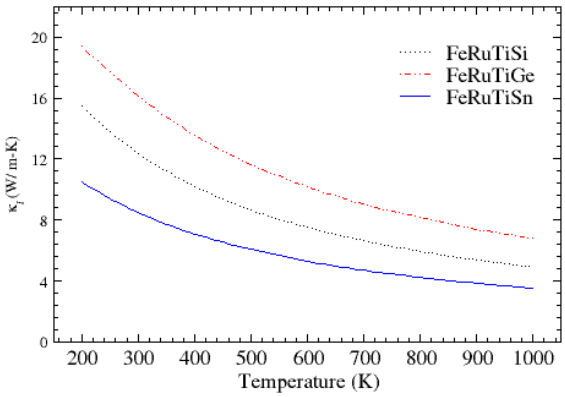

Figure 8. Lattice thermal conductivity (κ_l) as a function of temperature for FeRuTiSi, FeRuTiGe, and FeRuTiSn compounds.

Finally, the lattice thermal conductivity (κ_l) with respect to the temperature (200 – 1000 K) was computed for the three compounds (Figure 8). As expected, κ_l of FeRuTiSn is notably smaller than that of the two other congeners all over the temperature range. Nevertheless, a rather high κ_l is observed, especially at low temperature for all compounds, which is detrimental for a high *ZT*. With that respect, values computed here for our hypothetical compounds are comparable to those generally measured experimentally for QHAs [50]. However, a decreasing trend in κ_l with increasing temperature is noticed and values below 10 $Wm^{-1}K^{-1}$ are computed at high temperature. This decrease might be due to the excitation of phonon modes as the temperature increases which collectively induce more effective phonon scattering. Overall, the values of the total thermal conductivity in the case of FeRuTiSn are found to be the lowest ones in the entire temperature region under study. This is mainly due to the low frequency phonon modes available for both acoustic and optical branches which appear due to presence of the heavy elements Ru and Sn together. As a result, the lattice thermal conductivity at room temperature for FeRuTiSn (κ_l = ~7.6 $Wm^{-1}K^{-1}$) is nearly half of that reported by Choudhary et al. [100] for the Fe_2TiSn compound (κ_l = 14.8 $Wm^{-1}K^{-1}$). Interestingly, the rather low thermal conductivity computed for FeRuTiSn at high temperature (< 4 $Wm^{-1}K^{-1}$ at 900 K) compares well to that computed for the QHA CoFeTiAl (3.79 $Wm^{-1}K^{-1}$ at 900 K) [56]. Indeed, theoretical results reported here provide new possible materials for thermoelectric applications with suitable electronic structure and low thermal conductivity. These computationally guided results should be useful for experimental investigations on these materials in the near future.

3 Conclusions

In summary, we have here systematically investigated the structural, electronic, thermal and lattice thermal transport properties of the three hypothetical quaternary Heusler alloys FeRuTiX (X = Si, Ge, Sn) using first-principles calculations. This method has recently proven to be the more accurate method for first-principles electronic structure calculations of oxides, antimonide based superlattices, Heusler alloys, chalcogenides, carbides, nitrides, max-phase compounds, etc. [86–93]. All compounds are found to be non-magnetic with a semiconducting behavior with an indirect band gap character (ca. 0.5 eV at the TB-mBJ level of calculations). The flat band characteristics near the conduction band edge and the presence of degenerate multi-bands near the valance band edge suggest that these systems should exhibit both large Seebeck coefficients and electrical conductivity. The calculated vibrational spectra show thermal stability for all the compounds and predict the feasibility of sample synthesis. The computed lattice thermal conductivity indicates that among the three compounds that of FeRuTiSn shows a very small magnitude especially at high temperature. Indeed, a low lattice thermal conductivity (~3.5 $Wm^{-1}K^{-1}$ at 1000 K) together with a small electronic band gap (0.51 eV) with an appropriate electronic structure (disperse and flat bands) render FeRuTiSn a promising candidate as a high-temperature thermoelectric material. These theoretical findings should strongly encourage further experimental works in this direction.

4 Computational details

The all-electron full-potential augmented plane-wave (FP-LAPW) density-functional theory method implemented in the Wien2K code was used [76]. The density of states (DOS) and band structures were estimated using the equilibrium lattice parameters obtained from structural optimization of the lattice parameters of the unit cell of FeRuTiX (X = Si, Ge, Sn), within the LiMgPdSn structure ($F\bar{4}3m$, No. 216), with the atom position coordinates Fe (1/4,1/4,1/4), Ru (3/4,3/4,3/4), Ti (1/2,1/2,1/2), and X (0,0,0) [39]. The Perdew, Burke and Ernzerhof (PBE) functional was used for the exchange-correlation energy functional [77, 78]. Electronic structure results were also estimated using the Tran-Blaha modified Becke-Johnson (TB-mBJ) exchange functional as it has been found to provide better results for semiconductor compounds [79–82]. In the self-consistent field calculations, the value of energy/unit cell convergence was set to the 10^{-5} Ry. The energy cut-off and $R_{MT}K_{max}$ were set to –6.0 Ry and 7.0, respectively. The charge density was Fourier expanded up to the reciprocal vector G_{max} = –12 $Å^{-1}$. The *k*-point meshes for the structural optimization and electronic structure calculations were obtained from 15 × 15 × 15 and 20 × 20 × 20 grids, respectively. For the band structure plot, a total of 1000 *k*-points was used in the irreducible part of the Brillouin zone.

The thermal transport properties were calculated using the projector augmented-wave (PAW) method implemented in the Vienna Ab-initio Simulation Package (VASP) package [83]. The Perdew, Burke and Ernzerhof (PBE) functional was used for the exchange-correlation energy functional [77, 78, 84]. The kinetic energy cutoff for plane wave expansions was set to 500 eV, and a Brillouin zone sampling *k*-point mesh of 16 × 16 × 16 was used. Phonon density of states (PDOS) and phonon dispersions were estimated with the frozen phonon methods implemented in the PHONOPY package [85] using 2 × 2 × 2 supercells containing 32 atoms. The thermodynamic stability of the structures were checked by estimating the phonon frequencies of the acoustic and optical mode phonons along high symmetry directions within the framework of the force constant

method in which real-space force constants of the supercell are calculated by utilizing the density functional perturbation theory. Based on the first-principles linearized Boltzmann transport equation (LBTE) in single-mode relaxation time (SMRT) approximation, the lattice thermal conductivities were calculated using the PHONO3PY code [86] interfaced with the VASP code. The estimation of force constant was carried out using the density functional perturbation theory (DFPT) method [85] for the analysis of the phonon properties.

The equilibrium lattice constants and bulk modulii were fitted using the third-order Birch-Murnaghan equation of states (EOS) [87]:

$$E(V) = E_0 + \frac{9V_0B_0}{16}\left[\left\{\left(\frac{V_0}{V}\right)^{2/3} - 1\right\}^3 B_0' + \left\{\left(\frac{V_0}{V}\right)^{\frac{2}{3}} - 1\right\}^2 \left\{6 - 4\left(\frac{V_0}{V}\right)^{2/3}\right\}\right] \quad (1)$$

where E, V, V_0, B_0, and B_0' are the calculated energy, calculated volume, experimental volume of the unit cell, equilibrium bulk modulus, and pressure derivative of the bulk modulus, respectively.

Acknowledgements: S.S. acknowledges Ms. Sanchita Srivastav from Sri Satya Sai Vidya Vihar, Indore M.P. India, for helping in manuscript preparation and fruitful discussions. B.S acknowledges JSPS for the postdoctoral fellowship (P19720). T.M. acknowledges the funding from JSPS KAKENHI 19F19720, JP16H06441, and JST-Mirai JPMJMI19A1.

Author contributions: All the authors have accepted responsibility for the entire content of this submitted manuscript and approved submission.

Research funding: None declared.

Conflict of interest statement: The authors declare no conflicts of interest regarding this article.

References

1. Snyder, G.J.; Toberer, E.S.; Complex thermoelectric materials. In Materials for sustainable energy: a collection of peer-reviewed research and review articles from Nature Publishing Group, Dusastre, V (ed.), Nature Publishing Group, UK, 2011; pp.101–110.
2. He, J; Tritt, T.M. Advances in thermoelectric materials research: Looking back and moving forward. *Science* 2017, *357*, eaak9997.
3. Champier, D. Thermoelectric generators: A review of applications. *Energy Convers. Manag.* 2017, *140*, 167–181.
4. Zhao, D.; Tan, G. A review of thermoelectric cooling: materials, modeling and applications. *Appl. Therm. Eng.* 2014, *66*, 15–24.
5. He, R.; Schierning, G.; Nielsch, K. Thermoelectric devices: a review of devices, architectures, and contact optimization. *Adv. Mater. Technol.* 2018, *3*, 1700256.
6. Mori, T. Novel principles and nanostructuring methods for enhanced thermoelectrics. *Small* 2017, *13*, 1702013.
7. Mahan, G. D. Solid state physics. Academic Press, New York, 1998, 51, 11.
8. Muchtar, A.R.; Srinivasan, B.; Tonquesse, S.L.; Singh, S.; Soelami, N.; Yuliarto, B.; Berthebaud, D.; Mori, T. Physical Insights on the Lattice Softening Driven Mid-Temperature Range Thermoelectrics of Ti/Zr-Inserted SnTe—An Outlook Beyond the Horizons of Conventional Phonon Scattering and Excavation of Heikes' Equation for Estimating Carrier Properties. *Adv. Mater. Technol.* 2021, *11*, 2101122.
9. Byeon, D.; Sobota, R.; Delime-Codrin, K.; Choi, S.; Hirata, K.; Adachi, M.; Kiyama, M.; Matsuura, T.; Yamamoto, Y.; Matsunami, M.; Takeuchi, T. Discovery of colossal Seebeck effect in metallic Cu_2Se. *Nature Commun.* 2019, *10*, 72.
10. Choi, S.; Hiroi, S.; Inukai, M.; Nishino, S.; Sobota, R.; Byeon, D.; Mikami, M.; Matsunami, M.; Takeuchi, T. Effects of partial substitution by 5d heavy elements on the thermal transport in Fe_2VAl thin films. *Phys. Rev. B* 2020, *101*, 104312.
11. Chen, Z.G.; Han, G.; Yang, L.; Cheng, L.; Zou, J. Nanostructured thermoelectric materials: Current research and future challenge. *Prog. Nat. Sci.* 2012, *22*, 535–549.
12. Li, J.F.; Liu, W.S.; Zhao, L.D.; Zhou, M. High-performance nanostructured thermoelectric materials. *NPG Asia Mater.* 2010, *2*, 152–158.
13. Shi, X.L.; Zou, J.; Chen, Z.G. Advanced thermoelectric design: from materials and structures to devices. *Chem. Rev*. 2020, *120*, 7399–7515.
14. Moreno, J.J.G.; Cao, J.; Fronzi, M.; Assadi, M.H.N.; A review of recent progress in thermoelectric materials through computational methods. *Mater. Renew. Sustain. Energy* 2020, *9*, 1–22.
15. Wei, J.; Yang, L.; Ma, Z.; Song, P.; Zhang, M.; Ma, J.; Yang, F.; Wang, X.; Review of current high-ZT thermoelectric materials. *J. Mater. Sci.* 2020, *55*, 12642–12704.
16. Zhu, T.; Liu, Y.; Fu, C.; Heremans, J.P.; Snyder, J.G.; Zhao, X. Compromise and synergy in high-efficiency thermoelectric materials. *Adv. Mater.* 2017, *29*, 1605884.
17. Hinterleitner, B.; Knapp, I.; Poneder, M.; Shi, Y.; Müller, H.; Eguchi, G.; Eisenmenger-Sittner, C.; Stöger-Pollach, M.; Kakefuda, Y.; Kawamoto, N.; Guo, Q.; Baba T.; Mori T., Ullah S.; Xing-Qiu Chen.; Bauer E. Thermoelectric performance of a metastable thin-film Heusler alloy. *Nature* 2019, *576*, 85–90.
18. Shi, X.L.; Zou, J.; Chen, Z.G. Advanced thermoelectric design: from materials and structures to devices. *Chem. Rev*. 2020, *120*, 7399–7515.
19. Roychowdhury, S.; Ghosh, T.; Arora, R.; Samanta, M.; Xie, L.; Singh, N.K.; Soni, A.; He, J.; Waghmare, U.V.; Biswas, K. Enhanced atomic ordering leads to high thermoelectric performance in $AgSbTe_2$. *Science* 2021, *371*, 722–727.
20. Choi, S.; Hiroi, S.; Inukai, M.; Nishino, S.; Sobota, R.; Byeon, D.; Mikami, M.; Minamitani, E.; Matsunami, M.; Takeuchi, T. Crossover in periodic length dependence of thermal conductivity in 5d element substituted Fe_2VAl-based superlattices. *Phys. Rev. B* 2020, *102*, 104301.
21. Katayama, T.; Kim, S.W.; Kimura, Y.; Mishima, Y. The effects of quaternary additions on thermoelectric properties of TiNiSn-based half-Heusler alloys. *J. Elec. Mater.* 2003, *32*, 1160–1165.
22. Yadav, K.; Singh, S.; Takeuchi, T.; Mukherjee, K. Optical phonon modes assisted thermal conductivity in p-type ZrIrSb Half-Heusler alloy: A combined experimental and computational study. *J. Phys. D: Appl. Phys.* 2021, *54*, 495303.
23. Yadav, K.; Singh, S.; Muthuswamy, O.; Takeuchi, T.; Mukherjee, K., Unravelling the phonon scattering mechanism in Half-Heusler alloys $ZrCo_{1-x}Ir_xSb$ (x = 0, 0.1, and 0.25). *J. Phys.: Condens. Matter* 2022, *34*, 035702.
24. Silpawilawan, W.; Tanuslip, S.A.; Chetty, R.; Ohta, M.; Ohishi, Y.; Muta, H.; Kurosaki, K. Realizing Excellent n-and p-Type Niobium-

Based Half-Heusler Compounds Based on Thermoelectric Properties and High-Temperature Stability. *Adv. Elec. Mater.* 2020, *6*, 2000083.

25. Raghuvanshi, P.R.; Mondal, S.; Bhattacharya, A.; A high throughput search for efficient thermoelectric half-Heusler compounds. *J. Mater. Chem. A* 2020, *8*, 25187–25197.
26. Chauhan, N.S.; Raghuvanshi, P.R.; Tyagi, K.; Johari, K.K.; Tyagi, L.; Gahtori, B.; Bathula, S.; Bhattacharya, A.; Mahanti, S.D.; Singh, V.N.; Kolen'ko, Y.V. Defect Engineering for Enhancement of Thermoelectric Performance of (Zr, Hf) NiSn-Based n-type Half-Heusler Alloys. *J. Phys. Chem. C* 2020, *124*, 8584–8593.
27. Garmroudi, F.; Riss, A.; Parzer, M.; Reumann, N.; Müller, H.; Bauer, E.; Khmelevskyi, S.; Podloucky, R.; Mori, T.; Tobita, K.; Katsura, Y. Boosting the thermoelectric performance of Fe_2VAl− type Heusler compounds by band engineering. *Phys. Rev. B* 2021, *103*, 085202.
28. Everhart, W.; Newkirk, J. Mechanical properties of Heusler alloys. Heliyon, 2019; 5, e01578.
29. Galanakis I. Theory of Heusler and full-Heusler compounds. In: Heusler Alloys, Felser, C.; Hirohata, A. (eds.), Springer Series in Materials Science, Berlin, Germany: Springer, 2016, *222*, 3–36.
30. Hirohata A.; Kikuchi M.; Tezuka N.; Inomata, K.; Claydon, J. S.; Xu, Y. B.; Van der Laan, G. Heusler alloy/semiconductor hybrid structures. *Curr. Opin. Solid State Mater. Sci.* 2006, *10*, 93–107.
31. Hirohata, A.; Sukegawa, H.; Yanagihara, H.; Žutić, I.; Seki, T.; Mizukami, S.; Swaminathan, R. Roadmap for emerging materials for spintronic device applications. *IEEE Trans. Magn.* 2015, *51*, 0800511.
32. Jourdan, M.; Minár, J.; Braun, J.; Kronenberg, A.; Chadov, S., Balke, B.; Gloskovskii, A.; Kolbe, M.; Elmers, H.J.; Schönhense, G.; Ebert, H.; Felser, C.; Kläui, M. Direct observation of half-metallicity in the Heusler compound Co_2MnSi. *Nature Commun.* 2014, *5*, 3974.
33. Hirohata, A.; Sagar, J.; Fleet, L.R.; Parkin, S.S.P. Theory of Heusler and full-Heusler compounds. In: Heusler Alloys, Felser, C.; Hirohata, A. (eds.), Springer Series in Materials Science, Berlin, Germany: Springer, 2016, *222*, 219–248.
34. Elphick, K.; Frost, W.; Samiepour, M.; Kubota, T.; Takanashi, K.; Sukegawa, H.; Mitani, S.; Hirohata, A. Heusler alloys for spintronic devices: review on recent development and future perspectives. *Sci. Technol. Adv. Mater.* 2021, *22*, 235–271.
35. Tsujii, N.; Nishide, A.; Hayakawa, J.; Mori, T.; Observation of enhanced thermopower due to spin fluctuation in weak itinerant ferromagnet. *Sci. Adv.* 2019, *5*, eaat5935.
36. Bainsla, L; Suresh, K.G. Equiatomic quaternary Heusler alloys: A material perspective for spintronic applications. *Appl. Phys. Rev.* 2016, *3*, 031101.
37. Bradley, A.J; Rodgers, J.W. The crystal structure of the Heusler alloys. *Proc. Royal Soc. A* 1934, *144*, 340–359.
38. Kundu, A.; Ghosh, S.; Banerjee, R.; Ghosh, S; Sanyal, B. New quaternary half-metallic ferromagnets with large Curie temperatures. *Sci. Rep.* 2017, *7*, 1803.
39. Barman, C.K.; Mondal, C.; Pathak, B.; Alam, A. Quaternary Heusler alloy: an ideal platform to realize triple point fermions. *Phys. Rev. B* 2019, *99*, 045144.
40. Graf, T.; Felser, C.; Parkin, S.P.S. Simple rules for the understanding of Heusler compounds. *Prog. Solid State Chem.* 2011, *39*, 1–50.
41. Müchler, L.; Yan, B.; Casper, F.; Chadov, S.; Felser, C. Topological Insulators. In *Thermoelectric Nanomaterials*, Koumoto, K; Mori, T. (eds.), *Springer Series in Materials Science*, Springer-Verlag, Berlin, 2013, *182*, 123–139.
42. Beretta, D. Neophytou, N.; Hodges, J.M.; G. Kanatzidis, M.G.; Narducci, D.; Martin-Gonzalez, M.; Beekman, M.; Balke, B.; Cerretti, G.; Tremel, W.; Zevalkink, A.; Hofmann, A.I.; Müller, C.; Dörling, B.; Campoy-Quiles, M.; Caironi, M. Thermoelectrics: From history, a window to the future. *Mater. Sci. Eng. R Rep.* 2019, *138*, 210–255.
43. Felser, C.; Fecher, G.H.; Balke, B. Spintronics: a challenge for materials science and solid‐state chemistry. *Angew. Chem. Int. Ed.* 2007, *46*, 668–699.
44. Kumar, N.; Guin, S.N.; Manna, K.; Shekhar, C.; Felser, C. Topological Quantum Materials from the Viewpoint of Chemistry. *Chem. Rev.* 2021, *121*, 2780−2815.
45. Ma, J.; Feng, L.; Guo, R.; Liao, Y.; Khenata, R.; Liu, G.; Wang, L. New Half-Metallic Materials: FeRuCrP and FeRhCrP Quaternary Heusler Compounds. *Materials* 2017, *10*, 1367.
46. Guo, R.; Liu, G.; Wang, X.; Rozale, H.; Wang, L.; Khenata, R.; Wu, Z.; Dai, X. First-principles study on quaternary Heusler compounds ZrFeVZ (Z = Al, Ga, In) with large spin- flip gap. *RSC Adv.* 2016, *6*, 109394–109400.
47. Elahmar M.H.; Rached, H.; Rached, D.; Khenata, R.; Murtaza, G.; Bin Omran, S.; Ahmed, W.K. Structural, mechanical, electronic and magnetic properties of a new series of quaternary Heusler alloys CoFeMnZ (Z = Si, As, Sb): A first-principle study. *J. Magn. Magn. Mater.* 2015, *393*, 165–174.
48. De Paula, V.G.; Reis, M.S. All‐d‐Metal Full Heusler Alloys: A Novel Class of Functional Materials. *Chem. Mater.* 2021, *33*, 5483–5495.
49. Lue, C.S.; Chen, C.F.; Lin, J.Y.; Yu, Y.T.; Kuo, Y.K. Thermoelectric properties of quaternary Heusler alloys $Fe_2VAl_{1-x}Si_x$. *Phys. Rev. B* 2007, *75*, 064204.
50. Kara, H.; Kahaly, M.U.; Özdoğan, K. Thermoelectric response of quaternary Heusler compound CrVNbZn. *J. Alloys Compd.* 2018, *735*, 950–958.
51. Khandy, S.A; Chai, J.D. Robust stability, half-metallic ferrimagnetism and thermoelectric properties of new quaternary Heusler material: A first principles approach. *J. Magn. Magn. Mater.* 2020, *502*, 166562.
52. Lin, T.T.; Gao, Q.; Liu, G.D.; Dai, X.F.; Zhang, X.M.; Zhang, H.B. Dynamical stability, electronic and thermoelectric properties of quaternary ZnFeTiSi Heusler compound. *Curr. Appl. Phys.* 2019, *19*, 721–727.
53. Ilkhani, M.; Boochani, A.; Amiri, M.; Asshabi, M.; Rai, D.P. Mechanical stability and thermoelectric properties of the PdZrTiAl quaternary Heusler: A DFT study. *Solid State Commun.* 2020, *308*, 113838.
54. Lee, S.C. Robust mechanical stability, electronic structure, magnetism and thermoelectric properties of CoFeMnSb quaternary Heusler alloy: A first principle study. *J. Alloys Compd.* 2018, *742*, 903–909.
55. Haleoot, R.; Hamad, B. Thermodynamic and thermoelectric properties of CoFeYGe (Y = Ti, Cr) quaternary Heusler alloys: first-principles calculations. *J. Phys. Condens. Matter* 2019, *32*, 075402.
56. Enamullah.; Cha, P.R. The n-and p-type thermoelectric response of a semiconducting Co-based quaternary Heusler alloy: A density functional approach. *J. Mater. Chem. C* 2019, *7*, 7664–7671.
57. Elahmar, M.H.; Rached, H.; Rached, D.; Khenata, R.; Murtaza, G.; Omran, S.B.; Ahmed, W.K. Structural, mechanical, electronic and magnetic properties of a new series of quaternary Heusler alloys CoFeMnZ (Z = Si, As, Sb): A first-principles study. *J. Magn. Magn. Mater.* 2015, *393*,165–174.
58. Benkabou, M.; Rached, H.; Abdellaoui, A.; Rached, D.; Khenata, R.; Elahmar, M.H.; Abidri, B.; Benkhettou, N.; Bin-Omran, S. Electronic structure and magnetic properties of quaternary Heusler alloys CoRhMnZ (Z = Al, Ga, Ge and Si) via first-principles calculations. *J. Alloys Compd.* 2015, *647*, 276–286.
59. Elahmar, M.H.; Rached, H.; Rached, D.; Benalia, S.; Khenata, R.; Biskri, Z.E.; Omran, S.B. Structural stability, electronic structure and magnetic properties of the new hypothetical half-metallic

ferromagnetic full-Heusler alloy CoNiMnSi. *Mater. Sci.-Pol.* 2016, *34*, 8593–8602.

60. Gharbi, F.N.; Rabah, I.E.; Rabah, M.; Rached, H.; Rached, D.; Benkhettou, N.; Boukabrine, F. Theoretical Studies of the Structural, Electronic and Magnetic Properties of the CoFeCeZ (Z = P, As and Sb) Quaternary Heusler Alloys. *Spin* (World Scientific Publishing Company) 2020, *10*, 2050002.
61. Hoat, D.M.; Naseri, M. Examining the half-metallicity and thermoelectric properties of new equiatomic quaternary Heusler compound CoVRhGe under pressure. *Physica B Condens. Matter* 2020, *583*, 412058.
62. Rabah, I.E.; Rached, H.; Rabah, M.; Rached, D.; Benkhettou, N. A theoretical analysis of physical properties and half-metallic stability under pressure effect of the ScNiCrZ (Z = Ga, Al, In) Heusler alloys. *Spin* (World Scientific Publishing Company) 2021, *11*, 2150007.
63. Rached, H. Prediction of a new quaternary Heusler alloy within a good electrical response at high temperature for spintronics applications: DFT calculations. *Int J. Quantum Chem.* 2021, *121*, e26647.
64. Kozinsky, B.; Singh, D.J. Thermoelectrics by Computational Design: Progress and Opportunities. *Annu. Rev. Mater. Res.* 2021, *51*, 565–90.
65. Page, A.; P.F.P. Poudeu, P.F.P.; Uher, C. A first-principles approach to half-Heusler thermoelectrics: Accelerated prediction and understanding of material properties. *J. Materiomics* 2016, *2*, 104–113.
66. Gupta, Y.; Sinha, M.M.; Verma, S.S. Investigations of mechanical and thermoelectric properties of 'AlNiP' novel half-Heusler alloy. *Mater. Chem. Phys.* 2021, *265*, 124518.
67. Gheriballah, S.; Bouabdellah, B.; Oughilas, A.; Boukli, M.A.; Rahmoune, M.; Sayede, A. Investigating structure, magneto-electronic, and thermoelectric properties of the new d^0 quaternary Heusler compounds RbCaCZ (Z = P, As, Sb) from first-principles calculations. *Indian J. Pure Appl. Phys.* 2020, *58*, 818–824.
68. Venkateswara, Y.; Jadupati N.; Shanmukharao S. S.; Akhilesh K. P.; Babu P. D.; Varma M. R.; Nayak J.; Suresh K. G.; Alam. A. FeRhCrSi: Spin semimetal with spin-valve behavior at room temperature. *Physical Review B* 2023,107, L100401.
69. Prakash. R.; Kalpana, G. First-principles study on novel Fe-based quaternary Heusler alloys, with robust half-metallic, thermoelectric and optical properties. *RSC advances* 2023., 13, 0847-10860.
70. Bueno Villoro, R.; Zavanelli, D.; Jung, C.; Mattlat, D. A.; Hatami Naderloo, R.; Pérez, N.; Nielsch, K.; Snyder, G. J.; Scheu, C; He, R.; Zhang, S. Grain Boundary Phases in NbFeSb Half-Heusler Alloys: A New Avenue to Tune Transport Properties of Thermoelectric Materials. *Advanced Energy Materials* 2023, 2204321.
71. Özdoğan, K.; Şaşıoğlu, E.; Galanakis, I. Slater-Pauling behavior in LiMgPdSn-type multifunctional quaternary Heusler materials: Half-metallicity, spin-gapless and magnetic semiconductors. *J. Appl. Phys.* 2013, *113*, 193903.
72. Drews, J.; Eberz, U.; Schuster, H.U. Optische Untersuchungen an farbigen Intermetallischen Phasen. *J. Less-Common Met.* 1986, *116*, 271–278.
73. Guo, X.; Ni, Z.; Liang, Z.; Luo, H. Magnetic semiconductors and half-metals in FeRu-based quaternary Heusler alloys. *Comput. Mater. Sci.* 2018, *154*, 442–448.
74. Singh, S.; Singh, S.; Bijewar, N.; Kumar, A. Investigation of thermoelectric properties of magnetic insulator FeRuTiSi using first principle calculation. *AIP Conf. Proc.* 2020, *2265*, 030453
75. Guo, S.; Liu, Z.; Feng, Z.; Jia, T.; Anand, S.; Snyder, G.J.; Zhang, Y. Prediction of improved thermoelectric performance by ordering in double half-Heusler materials. *J. Mater. Chem. A* 2020, *8*, 23590–23598.
76. Blaha, P.; Schwarz, K.; Madsen, G.K.H.; Kvasnicka, D.; Luitz, J.; Laskowski, R.; Tran, F.; Marks, L.D. WIEN2k: An APW+lo program for calculating the properties of solids. *J. Chem. Phys.* 2020, *152*, 074101.
77. Perdew, J.P.; Wang, Y. Accurate and simple analytic representation of the electron-gas correlation energy. *Phys. Rev. B* 1992, *45*, 13244–13249.
78. Perdew, J.P.; Burke, K.; Ernzerhof, M. Generalized gradient approximation made simple. *Phys. Rev. Lett.* 1996, *77*, 3865–3868.
79. Tran, F.; Blaha, P. Accurate band gaps of semiconductors and insulators with a semi-local exchange-correlation potential. *Phys. Rev. Lett.* 2009, *102*, 226401.
80. Kumar, A.; Singh, S.; Patel, A.; Asokan, K.; Kanjilal, D. Thermoelectric properties of GaN with carrier concentration modulation: an experimental and theoretical investigation. *Phys. Chem. Chem. Phys.* 2021, *23*, 1601–1609.
81. Shastri, S.S.; Pandey, S.K. A comparative study of different exchange-correlation functionals in understanding structural, electronic and thermoelectric properties of Fe_2VAl and Fe_2TiSn compounds. *Comput. Mater. Sci.* 2018, *143*, 316–324.
82. Sk, S.; Devi, P.; Singh, S.; Pandey, S.K. Exploring the best scenario for understanding the high temperature thermoelectric behaviour of Fe_2VAl. *Mater. Res. Express* 2018, *6*, 026302.
83. Kresse, G.; Furthmüller, J. Efficient iterative schemes for ab initio total-energy calculations using a plane-wave basis set. *Phys. Rev. B* 1996, *54*, 11169–11186.
84. Kresse, G., Joubert, D. From ultrasoft pseudopotentials to the projector augmented-wave method. *Phys. Rev.* 1999, 59, 1758–1775.
85. Togo, A.; Tanaka, I. First principles phonon calculations in materials science. *Scr. Mater.* 2015, *108*, 1–5.
86. Togo, A.; Chaput, L.; Tanaka, I. Distributions of phonon lifetimes in Brillouin zones. *Phys. Rev. B* 2015, *91*, 094306.
87. Birch F. Finite elastic strain of cubic crystals. *Phys. Rev.* 1947, *71*, 809–824.
88. Rani, D.; Suresh, K.G.; Yadav, A.K.; Jha, S.N.; Bhattacharyya, D.; Varma, M.R.; Alam, A. Structural, electronic, magnetic, and transport properties of the equiatomic quaternary Heusler alloy CoRhMnGe: Theory and experiment. *Phys. Rev. B* 2017, *96*, 184404.
89. Alijani, V.; Winterlik, J.; Fecher, G.H.; Naghavi, S.S.; Chadov, S.; Gruhn, T.; Felser, C.; Quaternary Heusler compounds $Co_{2-x}Rh_xMnZ$ (Z= Ga, Sn, Sb): crystal structure, electronic structure, and magnetic properties. *J. Phys. Condens.* Matter 2012, *24*, 046001.
90. Aroyo, M.I.; Perez-Mato.; J.M., Capillas, C.; Kroumova, E., Ivantchev.; S., Madariaga, G.; Kirov, A.; Wondratschek, H. Bilbao Crystallographic Server: I. Databases and crystallographic computing programs. *Z. Kristallogr.* 2006, *221*, 15–27.
91. Aroyo, M.I.; Kirov, A.; Capillas, C.; Perez-Mato, J.M.; Wondratschek, H. Bilbao Crystallographic Server. II. Representations of crystallographic point groups and space groups. *Acta Crystallogr. A* 2006, *62*, 115–128.
92. Rached, Y.; Caid, M.; Rached, D.; Rached, H.; Benkhettou, N. Effects of stacking periodicity on the structural, electronic, optical and thermoelectric properties of GaSb/InSb superlattices. *Mater. Sci. Semicond. Process* 2023, *156*, 107297.
93. Meliani, S.; Kouidri, S.; Rached, H.; Keurti, M.E.; Moussa, M.O.; Slimane, A.B. First-principles prediction of asymmetric electronic structures, optoelectronic features, and efficiency for Sb_2S_3, Tl_2S, $TlSbS_2$, and $TlSb_3S_5$ compounds. *Solid State Commun.* 2022, *357*, 114973.
94. Belkacem, A.A.; Rached, H.; Caid, M.; Rached, Y.; Rached, D.; Mahmoud, N.T.; Benkhettou, N. The stability analysis and

efficiency of the new MAX-phase compounds M_3GaC_2 (M = Ti or Zr): A first-principles assessment. *Results Phys.* 2022, *38*, 105621.

95. Rached, Y.; Ait Belkacem, A.A.; Rached, D.; Rached, H.; Caid, M.; Merabet, M.; Benalia, S.; Djoudi, L.; Rabah, I.E.; Rabah, M. The Stability and Electronic and Thermal Transport Properties of New Tl-Based MAX-Phase Compound Ta_2TlX (X: C or N). *Phys. Status Solidi B* 2022, *259*, 2200195.

96. Bendriss, K.; Rached, H.; Ouadha, I.; Azzouz-Rached, A.; Chahed, A.; Bentouaf, A.; Rached, Y.; Rached, D. The stability, mechanical, electronic, and thermal features of the new superhard double transition-metal mono-nitrides and mono-carbides compounds. *Indian J. Phys.* 2023, *97*, 1125–1135.

97. Mancer, H.; Caid, M.; Rached, H.; Nakoul, Z.; Rached, D. Probing the effect of different exchange-correlation functionals on the optoelectronic features of chalcogenide compound Ag_2O. *Rev. Mex. de Fis.* 2023, *69*, 011004-1.

98. Rached, Y.; Rached, D.; Rached, H.; Cheref, O.; Caid, M.; Merabet, M.; Benalia, S.; Bourachid, I.; Djoudi, L. DFT assessment on stabilities, electronic and thermal transport properties of $CoZrSb_{1-x}Bi_x$ half-Heusler alloys and their superlattices. *Eur. Phys. J. Plus* 2023, *138*, 307.

99. Al-Qaisi, S.; Mushtaq, M.; Alzahrani, J.S.; Alkhaldi, H.; Alrowaili, Z.A.; Rached, H.; Haq, B.U.; Mahmood, Q.; Al-Buriahi, M.S.; Morsi, M. First-principles calculations to investigate electronic, structural, optical, and thermoelectric properties of semiconducting double perovskite Ba_2YBiO_6. *MNSC* 2022. *170*, 207397.

100. Choudhary, M.K.; Fjellvåg, H.; Ravindran, P. First principle studies on electronic and thermoelectric properties of Fe_2TiSn based multinary Heusler alloys. *Comput. Mater. Sci.* 2023, *216*, 111856.

10.1002/zaac.202300080

WILEY-VCH

ARTICLE

Entry for the Table of Contents (Please choose one layout)

Layout 1:

FULL PAPER

First-Principles Study on Electronic and Thermal Transport Properties of FeRuTiX Quaternary Heusler Compounds (X = Si, Ge, Sn)

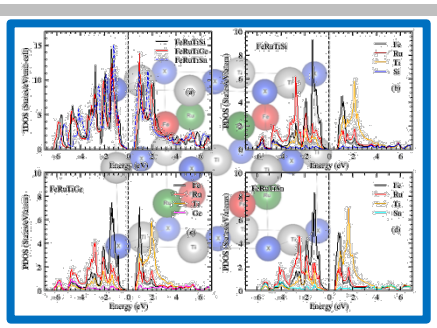

Saurabh Singh, Shubham Singh, Bhuvanesh Srinivasan*, Ashish Kumar, Nitinkumar Bijewar, Takao Mori, Tsunehiro Takeuchi and Jean-François Halet**

Page No. – Page No.

Title

Layout 2:

FULL PAPER

((Insert TOC Graphic here; max. width: 11.5 cm; max. height: 2.5 cm))

*Author(s), Corresponding Author(s)**

Page No. – Page No.

Title

Text for Table of Contents

WILEY-VCH

ARTICLE

Additional Author information for the electronic version of the article.

Saurabh Singh	ORCID identifier: 0000-0003-2209-5269
Shubham Singh	ORCID identifier: 0009-0002-1583-1918
Bhuvanesh Srinivasan	ORCID identifier: 0000- 0002-4472-2780
Ashish Kumar	ORCID identifier: 0000-0002-5240-3472
Takao Mori	ORCID identifier: 0000-0003-2682-1846
Tsunehiro Takeuchi	ORCID identifier: 0000-0001-9717-678X
Jean-François Halet	ORCID identifier: 0000-0002-2315-4200